



Hydrogel interfaced glass nanopore for high-resolution sizing of short DNA fragments



Muhammad Asad Ullah Khalid^a, Md. Ahsan Ahamed^a, Ming Dong^a, Aneesh Kshirsagar^a, Weihua Guan^{a,b,*}

^a Department of Electrical Engineering, Pennsylvania State University, University Park, PA, 16802, United States

^b Department of Biomedical Engineering, Pennsylvania State University, University Park, PA, 16802, United States

ARTICLE INFO

Keywords:
Short nucleic acid
Nanopore
Hydrogel
Multiplexed detection
PCR

ABSTRACT

Solid-state nanopores, known for their label-free detection and operational simplicity, face challenges in accurately sizing the short nucleic acids due to fast translocation and a lack of enzyme-based control mechanisms as compared to their biological counterparts with sizing resolutions still limited to ≥ 100 bp. Here, we present a facile polyethylene glycol-dimethacrylate (PEG-DMA) hydrogel interfaced glass nanopore (HIGN) system by inserting glass nanopore into the hydrogel to achieve sub-100 base pair (bp) resolution in short DNA sizing analysis. We systematically investigated the effects of hydrogel mesh size, spatial configurations of glass nanopores about the hydrogel, applied bias voltage, and analyte concentration on the transport dynamics of 200 bp double-stranded DNA (dsDNA). A 7.5 w/v% PEG-DMA hydrogel induced ~ 11 x increase in the mean dwell times compared with bare solution nanopore system. The insertion locations and depths of the glass nanopore into the hydrogel resulted in 7.16% and 5.28% coefficients of variation (CV) for mean normalized event frequencies. This enhancement of dwell times and invariability in translocation characteristics enables precise sizing of dsDNA fragments under 400 bp using HIGN, with an achieved size resolution of 50 bp with observable mean normalized peak amplitude ($\Delta I/I_0$) of ~ 0.005 . Furthermore, we have demonstrated the capability of HIGN to perform multiplex detection of influenza A virus (IAV) and severe acute respiratory syndrome-coronavirus-2 (SARS-CoV-2) through reverse transcriptase-polymerase chain reaction (RT-PCR). These results demonstrated the potential of HIGN as a versatile tool in nucleic acid analysis and multiplexed label-free molecular diagnostics.

1. Introduction

Nucleic acid (NA) sizing is a crucial analytical technique in molecular biology with widespread applications in forensic analysis(McCord et al., 2019), medical diagnosis(Barrio et al., 2021; Li et al., 2021), profiling and library preparation for next-generation systems (NGS) (Head et al., 2014), evaluation of gene editing efficiency(Fonfara et al., 2016), and detecting circulating tumor (ct) DNA (Lee et al., 2020) or cell-free (cf) DNA(Boutonnet et al., 2023; Ungerer et al., 2022). Solid-state nanopores have emerged as a powerful analytical tool for NA sizing due to their label-free nature and simplicity of operation (Al Sulaiman et al., 2018, 2021). The nanopore sizing of large DNA molecules is well-established. However, sizing shorter NA fragments using solid state nanopore sensors is limited by its poor size resolution and signal-to-noise-ratio (SNR), particularly at limited recording bandwidths. Moreover, the fast translocation rates (typically 10–100 nt/ns

for ssDNA and >10 bp/ μ s for dsDNA) of short NA fragments also limit the applicability of solid-state nanopores for certain applications like cfDNA, and ctDNA analysis (Folgea et al., 2005; Sanchez et al., 2021; Mouliere and Rosenfeld, 2015; Venkatesan and Bashir, 2011).

The commonly used lab-based techniques for the sizing analysis of NA fragments are gel electrophoresis (GE) (Green and Sambrook, 2019) and its modern successors, pulse field gel electrophoresis(Hashem et al., 2020; Herschleb et al., 2007), and capillary electrophoresis (CE) (Harstad et al., 2016), which separate them based on their size and charge. Despite certain advantages a CE may offer, the overall process is complex and time-consuming as it requires fluorescent dyes, high operating voltages (typically in kV), and an onsite fluorescence or UV detector. On the other hand, nanopore sizing is a simple and label-free process in which NA molecules are electrokinetically translocated between two salt buffer solutions through the nanosized orifice in the presence of a relatively low electric field (typically in hundreds of

* Corresponding author. Department of Electrical Engineering, Pennsylvania State University, University Park, PA, 16802, United States.

E-mail address: wzg111@psu.edu (W. Guan).

millivolts), producing a detectable ionic current blockade (Fragasso et al., 2020; Venkatesan and Bashir, 2011). However, poor size resolution and SNR limit its effectiveness in accurately sizing short NA fragments. Some amplification techniques and the use of additional probes have been integrated with the nanopore sensor to enhance the SNR (Ahamed et al., 2023). Nevertheless, the rapid translocations of DNA molecules remain a challenge, with solutions focusing on altering spatiotemporal scales through high-capability detection instruments (Larkin et al., 2014) or by decelerating the translocating molecules.

Hydrogel materials when filled or interfaced with solid state nanopores have significantly slowed down DNA translocations as observed by (Al Sulaiman et al., 2018) with size resolution reaching ~100 bp highlighting their potential for cfDNA fragment analysis as well (Al Sulaiman et al., 2021). Although filling the nanopores with hydrogels is a promising approach for NA sizing, it can be tedious and may result in a high failure rate because of the post-filling cross-linking process. In recent work (Khatri et al., 2023) capitalized on the nanoconfinement effect of double-barreled nanopores on the cis side and crowding enhanced by the fibrin hydrogel on the trans side for single molecule detection with sizes as small as 1 nm, including nucleoside triphosphates (ATP and dCTP), short peptides, and small proteins (ferritin and insulin). However, they did not study the nucleic acid sizing capability of their platform. Another work demonstrated the enhanced detection of 3.5 kbp circular and linearized DNA plasmids using macromolecular crowding effect of 50% PEG 8000 electrolyte bath solution (Chau et al., 2020). Although they observed enhanced detection of DNA plasmid with peak amplitudes reaching 6-fold in crowded conditions, they didn't explore its applicability to size short DNA fragments. In a later work they were able to obtain a sizing resolution of ~500 bp with a polymer-electrolyte solution of CsBr and PEG 35K (Chau et al., 2022). Recently, bare solution glassy nanopores have shown promise for sizing short DNA fragments by leveraging the DNA charge neutralizing effect of Li⁺ ions (Kowalczyk et al., 2012) in high concentration 4 M LiCl salt solution (Li et al., 2023). Despite its promising capabilities, the sizing resolution was limited to 200 bp. So far hydrogel based nanopores have shown potential for precise sizing of short DNA fragments with high resolution, but there is still lack of a facile hydrogel-assisted glass nanopore platform to achieve sub-100 bp sizing resolution.

In this work, we have developed a facile PEG-DMA hydrogel-interfaced glass nanopore (HIGN) platform by inserting nanopore into the hydrogel, aiming to perform label-free nucleic acid sizing and counting to achieve sub-100 bp resolution. We leverage the charge neutralizing effect of high salt concentration 4 M LiCl electrolyte reinforced with hydrogel barrier to significantly slow down the translocations of DNA fragments as short as 50 bp. We showed an effective over tenfold increase in dwell times by the slow-down of molecular translocations as compared with a bare solution nanopore when short dsDNA fragments were electrokinetically moved from a glass nanopore with 10 nm diameter into the 7.5% PEG-DMA hydrogel. The 7.5% HIGN also demonstrated higher mean peak amplitudes, and event frequency when compared to a 5% HIGN. The detailed analysis of the spatial configurations of glass nanopore into the PEG-DMA hydrogel, in terms of insertion locations and depths, implied negligible changes in the translocation characteristics of 200 bp dsDNA molecules with mean normalized frequencies characterized by coefficient of variation. The resolution of HIGN was determined by testing dsDNA targets with lengths ranging from 50 bp to 400 bp. We further demonstrated the suitability of our HIGN for the multiplexed detection of IAV and SARS-CoV-2 respiratory infections from a multiplexed RT-PCR reaction.

2. Materials and Methods

2.1. Materials and chemicals

Quartz capillaries (Q100-50-7.5), with inner and outer diameters of 0.5 and 1 mm, respectively, were purchased from Sutter Instrument,

USA. The Pipette holder (QSW-T10N) was purchased from Warner Instruments. Ag/AgCl electrodes were homemade with 0.2 mm Ag wires (Warner Instruments, USA). A microinjector (MF34G-5) was purchased from World Precision Instruments. Lithium Chloride (LiCl) salt, Tris-EDTA-buffer solution (pH 8.0), Polyethylene glycol dimethacrylate (PEG-DMA) (M_n: 1000), ammonium persulfate (APS), N,N,N',N'-Tetramethylethylenediamine (TEMED), sulfuric acid (H₂SO₄) and hydrogen peroxide (H₂O₂) were purchased from Sigma-Aldrich. The dsDNA fragments of various lengths (50–400 bp), SARS-CoV-2 primers mix and UltraPure™ DNase/RNase-Free Distilled Water (Catalog number: 10977015) were purchased from Thermo Fisher. Gel Loading Dye, Yellow (6X) was obtained from NEW ENGLAND Biolabs Inc. (NEB). The qScript XLT 1-Step RT-qPCR ToughMix was acquired from Quantabio. Agarose gel (#BP160-500) was purchased from Fisher Scientific, and all the other oligos used were acquired from Integrated DNA Technologies, Inc.

2.2. Nanopore fabrication

Quartz capillaries were first cleaned with piranha solution to remove organic residues. Piranha solution was custom prepared in the lab by mixing H₂SO₄ and H₂O₂ in 3:1. Piranha-cleaned capillaries were rinsed with DI water and vacuum dried at 120 °C for 20 min. Each capillary was then subjected to an oxygen plasma cleaning cycle to enhance hydrophilicity before laser-pulling (Dong et al., 2022). A one-line recipe, “heat 650, filament 5, velocity 50, delay 140, and pull 165”; was used to pull the capillaries with a laser pipet puller (P-2000, Sutter Instruments, USA) (Ahamed et al., 2023; Lastra et al., 2022). This laser-pulling recipe fabricates typically sub 10 nm pores and the pore size was controlled by observing the fabrication time from the pipet puller instrument and the IV curve in a free measurement buffer solution. The pulling parameters are instrument specific and the fabrication process is sensitive to physical conditions of the environment. They may result in nanopores with slightly different diameters, so a custom protocol should be adapted to ensure a specific nanopore diameter. 4 M LiCl measurement buffer solution was prepared by dissolving LiCl in Tris-EDTA (pH 8.0) buffer and filtered using 0.2 μm syringe filter (Whatman Puradisc, PES sterile).

2.3. Synthesis of PEG-DMA hydrogel

The chemical cross-linking synthesis protocol of PEG-DMA hydrogel was adopted and slightly modified from (Acharya et al., 2020) as shown in Fig. S1. Briefly, PEG-DMA (M_n: 1000) was dissolved in the 2 M LiCl, 10 mM Tris-EDTA (pH 8.0) solution, at desired % w/v. The gel precursor solution was vortexed thoroughly to ensure complete dissolution and then sonicated for at least 10 min. APS solution and tetramethylethylenediamine (TEMED) were added to the Gel precursor solution with final concentrations of 10 mM and 15 mM, respectively. The gel solution was immediately pipetted into the sample tubes and then allowed to polymerize for 1 h. After polymerization, 60 μL of measurement buffer was pipetted into the hydrogel for swelling and balancing measurement buffer solution concentrations on both sides. Hydrogels were allowed to swell for at least 48 h before use.

2.4. Hydrogel characterizations

The disk-shaped hydrogel samples were synthesized according to the above-mentioned protocol. They were cut to expose cross-sections with sharp blades. These cross-section samples were then immersed in serially increasing (30%, 50%, 70%, and 100%) concentrations of isopropyl alcohol (IPA) for dehydration for 30 min each. The partially dehydrated cross-section samples were then quickly frozen by immersing in liquid nitrogen for 1 h and later subjected to lyophilization at -50 °C for 4 h. The lyophilized cross-sections of hydrogel prototypes were then observed under a scanning electron microscope (SEM – thermoscientific Verios G4 UC) at different magnifications to observe the mesh structure.

2.5. RT-PCR assay

Single plex IAV: The RT-PCR reaction was conducted in a total volume of 20 μL . It includes 0.15 μL of 20 μM concentration both forward and reverse primers (Table S1). To prepare the reaction mixture, 10 μL of 2 \times qScript XLT Master Mix, 7.70 μL of nuclease-free water, and 2 μL of RNA sample were added. Details of the recipe are provided in Table S3. The RT-PCR was performed on the Bio-Rad CFX96 system, which followed a thermal cycle starting with a reverse transcription for 10 min, an initial denaturation at 95 °C for 1 min, and 35 cycles of 10 s at 95 °C for denaturation and 20 s at 63 °C for primer annealing.

Single plex SARS-CoV-2: The RT-PCR reaction was carried out in a total volume of 20 μL . It includes 1.5 μL of the mixed primers (Table S2). To this mixture, 10 μL of 2 \times qScript XLT Master Mix, 6.5 μL of nuclease-free water, and 2 μL of RNA sample were added with the same thermal cycling conditions described above. Details of the recipe are provided in Table S3.

Multiplexed IAV + SARS-CoV-2: In the multiplexed RT-PCR, the

reaction's total volume was also 20 μL , with 0.15 μL of each primer at 20 μM concentration. The reaction mixture contained 10 μL of 2 \times qScript XLT Master Mix, 4.20 μL of nuclease-free water, and 2 μL of each RNA sample, with the same previous thermal cycling conditions. Details of the recipe are in Table S4.

Gel analysis: Following the RT-PCR reaction, the products were separated on a 5% agarose gel electrophoresis, stained with SYBR™ Safe DNA Gel Stain, and operated at 80 V for 60 min. The desired bands were imaged and analyzed using the BIO-RAD GelDoc Go Imaging System with a 10 s exposure time.

2.6. Data acquisition and analysis

All ionic current-time ($I-t$) data were acquired at 100 kHz sampling frequency using a patch clamp amplifier Axopatch 200B by Molecular Devices, an NI 6363 DAQ card, and a low pass filter (5 kHz) in a custom LabVIEW program. Data were further analyzed using a custom MATLAB script to extract peak information like current blockade peak

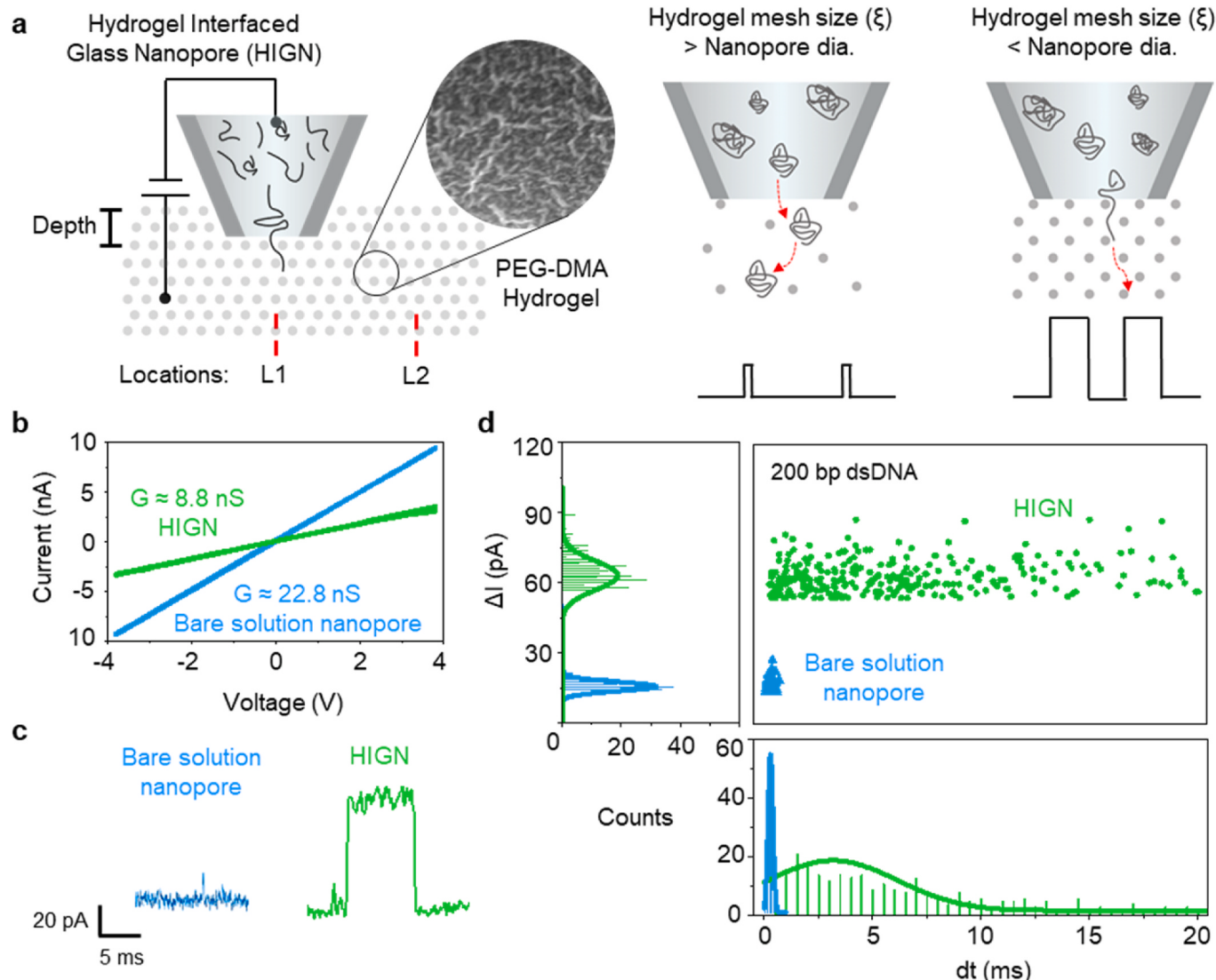


Fig. 1. Working mechanism of HIGN: (a) Schematic configuration of HIGN showing the entropic interactions of translocating DNA molecule with PEG-DMA hydrogel mesh fibers under the influence of an applied negative bias when glass nanopore is inserted into the hydrogel; a linear threading movement is only observed when hydrogel mesh size (ξ) is greater than the glass nanopore diameter, (b) IV curves show a ~61% reduction in open pore conductance values for the HIGN (8.8 nS) as compared to a bare-solution nanopore (22.8 nS), data presented as presented as $\mu \pm \sigma$ for $n = 3$, (c) representative event shapes for a 200 bp dsDNA molecule suggest an increase of ~4 \times in event peak amplitude and ~11 \times in dwell time for HIGN as compared to a bare-solution nanopore, (d) event scatter plot comparison of HIGN and bare-solution nanopore with respective dwell time and peak amplitude distributions.

amplitudes, dwell times, and counts. All the measurements were repeated with at least three HIGN for statistical evaluation.

3. Results and discussion

3.1. Working mechanism of HIGN

To facilitate the nanopore-based sizing of short nucleic acid fragments, a facile HIGN platform was developed by inserting the glass nanopore into a chemically cross-linked 7.5% w/v PEG-DMA hydrogel. We propose that a short DNA molecule encounters significant entropic barriers at the hydrogel-nanopore interface offered by the hydrogel mesh fibers, before completely exiting from the nanopore. The size of the hydrogel mesh (ξ) is carefully selected to be smaller than the nanopore diameter to force DNA molecules to thread through the nano-confinements of the hydrogel mesh structure. This increases the dwell time of the nucleic acid fragment in the nanopore, thereby producing a detectable ionic current blockade as compared to a bare measurement salt buffer. An increase in the current blockade amplitudes, however, has been pre-established by the crowding enhanced detection of DNA molecules by (Chau et al., 2020). The Ag/AgCl electrodes were inserted in both the hydrogel and the glass nanopore to establish the electric field with Axopatch 200B amplifier for ionic current data recording. A schematic representation of this whole mechanism has been shown in Fig. 1a. Glass nanopore was fabricated by laser-pulling with an estimated pore diameter of 10 nm as described in section 2.2 of the “Materials and Method”, whereas the PEG-DMA hydrogel was chemically cross-linked, as described in Fig. S1, with an estimated mesh size of ~7 nm, determined by the Peppas-Merrill equation (Carr and Peppas, 2009) given below.

$$\xi = \delta^{-1/3} (2C_n M_c / M_r)^{1/2} l \quad (1)$$

Where ξ denotes the mesh size, and δ , C_n , M_c , M_r , l , denote reciprocal of swelling ratio, Flory characteristic ratio of the polymer, the molecular weight between cross-links, the molecular weight of the repeat unit, and the bond length of a carbon-carbon bond (1.54 Å), respectively.

PEG-DMA hydrogel was chosen because of its high hydrophilicity (Burke et al., 2019) and ultra-low molecular adsorption (Kubo et al., 2015). These properties are desirable to ensure high swelling rates and efficient molecular transport which are not the characteristics of hydrophobic gels. A quick current-voltage (IV) sweep analysis from Fig. 1b compares open pore conductance values for both bare solution and hydrogel-interfaced nanopores for three bare solution and three hydrogel samples ($n = 3$). Nearly 61% reduction in conductance values was observed when the glass nanopore was inserted into the PEG-DMA hydrogel as compared to the bare solution nanopore, which can be attributed to the confined volumes of the measurement buffer within the mesh fibers of the hydrogel. A 200 bp dsDNA target was analyzed with both bare solution nanopore and HIGN to compare the DNA translocation characteristics. A $\sim 4 \times$ increase in peak amplitude as well as $\sim 11 \times$ increase in dwell time can be seen in current in Fig. 1c from the representative translocation events when the nanopores were used in eject configuration by applying negative bias (-0.2 V) to the glass nanopore. A 5 s current time ($I-t$) trace for HIGN in Fig. S2 shows a stable baseline with no translocation signal when no DNA target is present. On the contrary, another 5 s $I-t$ trace just below that one shows high frequency of translocations for 200 bp dsDNA target. An event scatter has been plotted for both bare solution nanopore and HIGN in Fig. 1d, with a clear difference in both scatter populations. To further elaborate on this, counts' distributions for event amplitudes and dwell times have also been presented. Peak amplitude counts have been fitted with Gaussian distributions with a mean of 15.7 pA for bare solution nanopore, as compared to a 63.2 pA for HIGN. Similarly, the dwell times follow Poisson and Gaussian distributions for bare-solution and HIGN with mean of 0.29 ms and 3.18 ms (an increase of $\sim 11 \times$ compared to bare

solution nanopore), respectively. This analysis suggests an increase not only in the dwell times but also in the mean peak amplitudes for short dsDNA translocations. Despite a significant increase in mean peak amplitude and dwell time, the hydrogel properties may still alter these characteristics. We sought to evaluate the performance of HIGN with different hydrogel % w/v.

3.2. Characterizations of PEG-DMA hydrogel

Hydrogel mesh size is a critical parameter to control the translocations of dsDNA, which can be tuned by varying the % w/v of PEG-DMA crosslinker in the precursor hydrogel solution. The hydrogel synthesis and characterization methods have been described previously in sections 2.3 and 2.4 of “Materials and Methods”. To perform morphological characterization of the mesh network, 5, 7.5, and 10% w/v PEG-DMA hydrogel prototypes were prepared in Tris-EDTA buffer only with Peppas-Merrill estimated mesh sizes (15, 7 and 3 nm respectively) comparable to the nanopore diameter (10 nm). The cross-sections of these hydrogels were observed using a “Verios” field emission scanning electron microscope (FESEM), as shown in Fig. 2a–c. The mesh structure was clearly visible at higher magnifications (images with 500 nm scale bar) and became denser with increasing % w/v of the PEG-DMA cross-linker. The hydrogel mesh structures were not visible at lower magnifications, as evident from Fig. S3. All the hydrogel prototypes were tested to analyze the translocation characteristics of a 200 bp dsDNA target. The respective $I-t$ traces in Fig. 2d show the reliable operation for 5% and 7.5% w/v hydrogels with event frequency increasing as with the hydrogel % w/v. This can be explained by the molecular crowding (Chau et al., 2020, 2022; Khatri et al., 2023) experienced by translocating DNA molecules from increased entropic barriers of high polymer %w/v causing increased accumulation of these molecules at the hydrogel nanopore-interface before exit. The macromolecular crowders like PEG have been shown to increase the peak amplitudes and event frequencies with their increasing concentrations in the polymer-electrolyte solutions due to their signal enhancement effect caused by the reversal of negative ion current rectification and salt-gradient dependent disruption of electroosmotic flow (Rabinowitz et al., 2019; Yusko et al., 2010). A similar dual-effect is seemingly responsible for this increase in the peak amplitudes and event frequency when the %w/v of PEG-DMA hydrogel increases from 5% to 7.5% as the translocating dsDNA now encounters increased entropic barriers causing higher salt concentration gradient and disrupted electrophoretic flow. But the 10 % w/v HIGN was getting frequently clogged, as evidenced by its $I-t$ trace and high noise. The IV curves of the 5%, 7.5%, 10% (HIGN) have also been shown in Fig. 2e for 3 different prototypes of each hydrogel % w/v sample ($n = 3$). As expected, the conductance of the HIGN decreases with increasing % w/v of PEG-DMA. The conductance value dropped by $\sim 67.4\%$ for 10% w/v hydrogel when compared to 5% w/v hydrogel. This further confirms the presence of proportioned hydrogel entropic barriers at the hydrogel-nanopore interface.

The cross-linking method of hydrogel can greatly affect the physical or chemical properties of the hydrogels obtained. For example, the hydrogels synthesized using a physical cross-linking method lack in mechanical strength and stability as compared to the ones synthesized using a chemical cross-linking method. According to sieving mechanisms in gel electrophoresis (Chung et al., 2014; Fu et al., 2008) the hydrogel mesh size should be smaller than or comparable to the gyration radius (variable for each DNA length) of the molecule to be transported, the persistence length (fixed at ~ 50 nm for ~ 150 bp dsDNA length), and the nanopore diameter for effective slowdown of the translocation. This is why hydrogel mesh sizes and hence the % w/v under study should be chosen carefully to aim for effective slowdown of short DNA fragments. For this work, we synthesized three different hydrogel prototypes with 5, 7.5, and 10% w/v. The selection of these particular percentages was aimed at obtaining estimated hydrogel mesh sizes of ~ 15 , 7, and 3 nm a bit larger, comparable, and smaller than our nanopore diameter (10 nm)

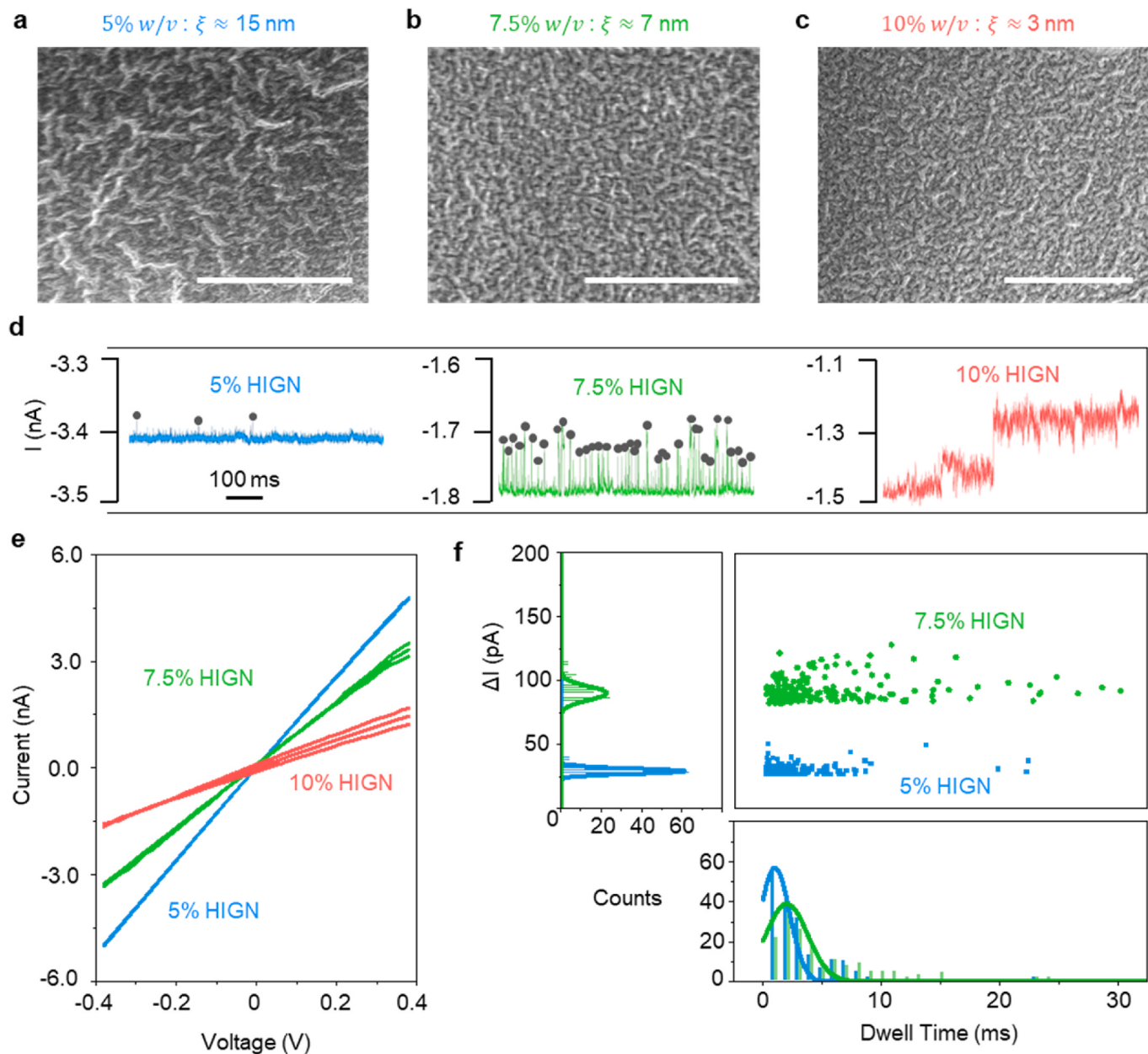


Fig. 2. PEG-DMA hydrogel characterizations: SEM images of PEG-DMA hydrogel for (a) 5% w/v, (b) 7.5% w/v and (c) 10% w/v with mesh size (ξ) estimations, scale bars are 500 nm, (d) $I-t$ traces for different %w/v HIGN showing high noise and partial clogging for 10 % w/v hydrogel. (e) IV sweeps show decreasing conductance values for increasing gel % in HIGN, presented as $\mu \pm \sigma$ for $n = 3$, (f) effect of hydrogel % w/v and hence the mesh size on the translocation characteristics of a 200 bp dsDNA target.

respectively. We anticipate a considerable slowdown of DNA translocations for hydrogel prototypes containing 7.5, and 10% w/v PEG-DMA crosslinker, however all the hydrogels were characterized for critical evaluation of the translocation characteristics of 200 bp dsDNA. The 200 bp target observed higher dwell times indicated by the scatter plot population from 5% w/v HIGN with a mean of 2.8 ms in Fig. 2f. But they significantly increased to ~6.2 ms when 7.5% w/v HIGN was used. This can be understood from the finer mesh (with a ξ of ~7 nm) offering increased retarding force to the translocating DNA. Similarly, as a result, an increase in peak amplitudes could also be observed for 7.5% w/v HIGN as compared to 5% HIGN. This led us to carry out the rest of the experimental analysis using a 7.5% w/v hydrogel. The choice of 7.5% w/v hydrogel is also complementing a 10 nm glass nanopore diameter, which may change accordingly for other glass nanopore diameters. We did not consider 10% w/v hydrogel for further analysis because of its

high noise and frequent clogging issues.

3.3. Effect of spatial placement, applied bias, and target concentration on translocation characteristics of 200 bp NA fragments

Since the hydrogel mesh structure has an inherent degree of heterogeneity (Di Lorenzo and Seiffert, 2015; Lalitha Sridhar et al., 2017; Malo De Molina et al., 2015) and it has been swollen in the 4 M LiCl Tris-EDTA measurement buffer before analysis, the spatial placements of nanopores are expected to affect the translocation characteristics of the nucleic acid molecules in HIGN. Moreover, the applied bias on the patch electrode and target concentrations can also alter these characteristics (Nouri et al., 2019). To evaluate the effect of inherent heterogeneity of the hydrogel mesh structure on the DNA translocation characteristics, the nanopore filled with a 200 bp dsDNA was spatially

placed at different insertion locations and depths as graphically demonstrated in Fig. S4a. A $\pm 1 \mu\text{m}$ precision XYZ micro-positioner was used to control the glass nanopore movement along all three axes when interfaced with the hydrogel. The effect of these control parameters was evaluated in terms of event scatter plots, and event frequency, as shown in Fig. 3. To analyze the effect of different insertion locations (L1, L2, L3, L4), the applied bias potential was fixed at -0.2 V and insertion depth at $60 \mu\text{m}$. As can be seen from the representative $I-t$ traces in Fig. 3a and the different scatter populations in Fig. 3b, the different insertion locations do not affect the peak amplitudes and dwell times significantly. The interval time distributions for different insertion locations shown in Fig. S4b (fitted by mono-exponential fit, $P_C(t) = A \exp(-t/\tau)$) also

demonstrate negligible shift which can be related to the normalized event frequencies shown in Fig. 3c. The mean normalized event frequencies (for three different hydrogel prototypes, $n = 3$) for four different insertion locations showed only a 7.16% CV suggesting negligible variability and high precision.

To assess the effect of insertion depths on the translocation characteristics of the DNA molecules, the applied bias at the patch electrode and insertion location of the nanopore into the hydrogel were fixed at -0.3 V at L1 respectively. The glass nanopore was inserted at three different insertion depths (D1: $30 \mu\text{m}$, D2: $60 \mu\text{m}$, D3: $120 \mu\text{m}$) progressively one by one as shown in Fig. S4a. A quick look at the $I-t$ traces for different insertion depths, shown in Fig. 3d, suggests insignificant

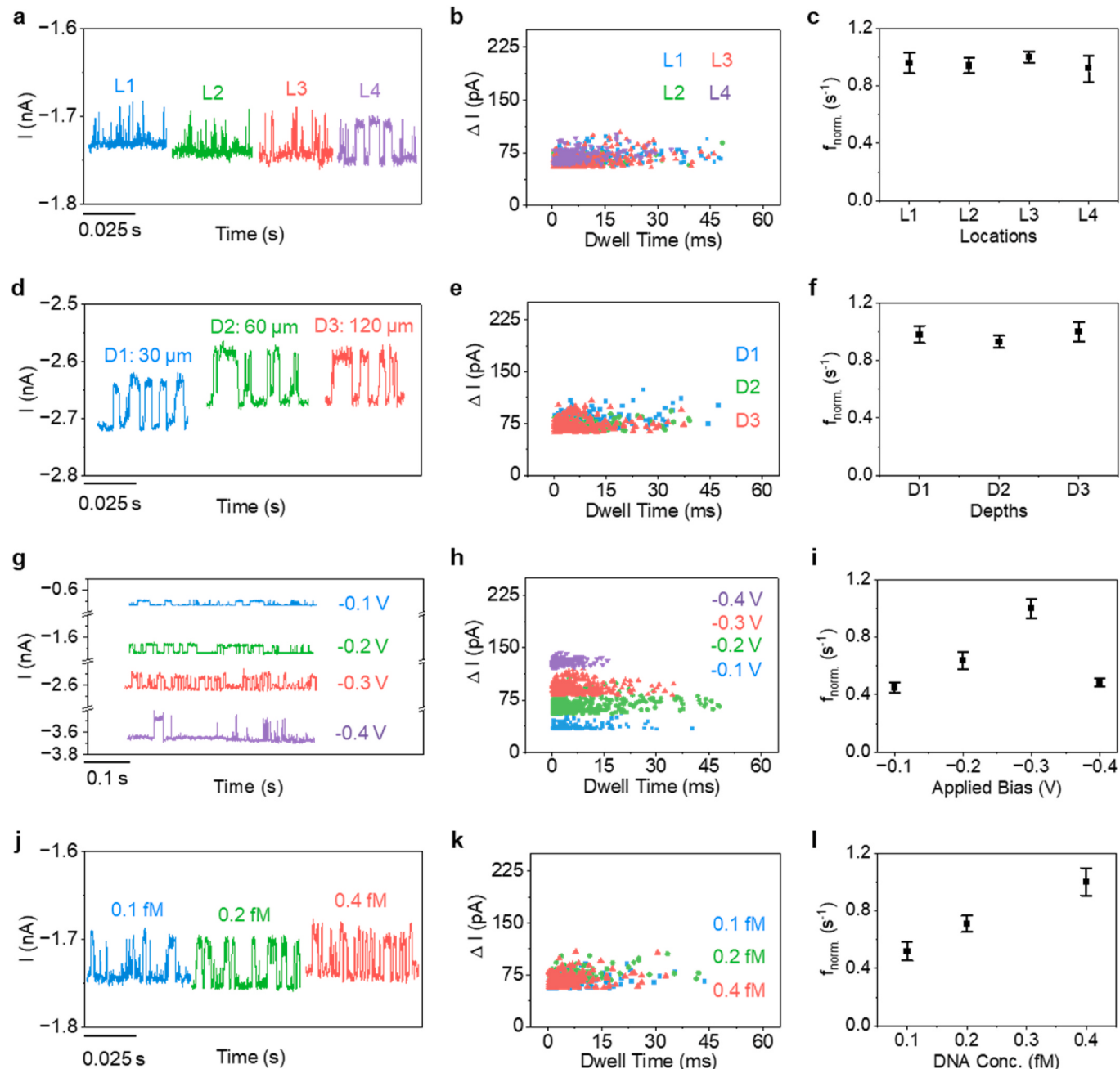


Fig. 3. Effect of spatial placements and experimental conditions on the translocation characteristics of 200 bp dsDNA: (a–c) different insertion locations (L1, L2, L3, L4), but fixed insertion depth of (D2: $60 \mu\text{m}$) and applied bias (-0.2 V), (d–f) different insertion depths (D1: $30 \mu\text{m}$, D2: $60 \mu\text{m}$, D3: $120 \mu\text{m}$) but fixed insertion location (L1) and applied bias (-0.3 V), (g–i) different applied bias (-0.1 V , -0.2 V , -0.3 V , -0.4 V) but fixed insertion location (L1) and depth (D2: $60 \mu\text{m}$), (j–l) different target concentrations (0.1 fM , 0.2 fM , 0.4 fM) but fixed insertion location (L1), depth (D2: $60 \mu\text{m}$) and applied bias (-0.2 V); the subplots indicate respective event rates. Normalized event rates have been presented as $\mu \pm \sigma$ for $n = 3$.

variations in the blockade amplitudes and dwell times but slight shift in the baseline current. The slight variations of $\pm 5\%$ in the baseline current are not expected to significantly alter the translocation characteristics of the DNA molecules. This was further confirmed by the indistinguishable populations for three different depths in the event scatter plot shown in Fig. 3e. Similarly, the event frequencies were expected to remain unchanged (for three different hydrogel prototypes, $n = 3$), which is evident from Fig. 3f with respective interval time distributions shown in Fig. S4c. The mean normalized event frequencies (for three different hydrogel prototypes, $n = 3$) for three different insertion depths showed only a 5.28% CV also suggesting negligible variability and high precision. A further analysis of a deeper insertion depth of 200 μm caused the nanopore to clog immediately due to the poor swelling of the hydrogel deep down. This is expected because hydrogel swelling is a time dependent process. Although not desirable at this point, if the hydrogel is allowed to swell for longer than 48 h, the workable insertion depth may also increase.

To further explore the effect of the applied bias voltage, both the insertion location and depth were fixed to be L1 and D2 respectively. The applied bias on the patch electrode was increased from -0.1 V up to -0.3 V , and an increase in event frequency was observed as shown in I - t profiles in Fig. 3g and event frequencies in Fig. 3i (for three different hydrogel prototypes, $n = 3$). This increase in event frequencies can be understood from the scatter plot in Fig. 3h and electrophoretic force theory. Initially, at -0.1 V , the electrophoretic force is not sufficient to drive many DNA molecules through the nanopore into the PEG-DMA hydrogel, so the event frequency is low. But as this applied bias is increased from -0.1 V to -0.2 V , the event frequency increases as the electrophoretic force increases causing a higher number of DNA translocations. However, the effect of higher electrophoretic force becomes visible when the applied bias is increased from -0.2 V to -0.3 V when dwell times start to decrease, as can be seen in Fig. 3h, but the event frequency still increases as the translocations are still in the detectable range. Finally, when the applied bias is increased further to -0.4 V , the dwell times decrease significantly, allowing some of the DNA translocations to go undetected, thereby decreasing event frequency. The corresponding interval time distributions in Fig. S4d also complemented this phenomenon, where the slope for -0.4 V is even less than -0.1 V applied bias. Hence, increasing the applied bias up to -0.3 V decreased mean dwell times, increased mean peak amplitudes and normalized event frequencies in a predictable manner. A similar phenomenon is expected for dsDNA target lengths closer to 200 bp on either side, however it may not hold true for lengths much longer or shorter than 200 bp. And the scope of this work is limited to short DNA fragments with lengths in 50–400 bp range only.

The effect of target concentrations was also analyzed at fixed applied bias of -0.2 V , insertion location L1 and insertion depth D2. I - t traces, scatter populations, and normalized event frequencies (for three different hydrogel prototypes, $n = 3$) have been shown in Fig. 3j-l for different target concentrations (0.1 fM , 0.2 fM , 0.4 fM) with respective interval time distributions in Fig. S4e. The alterations in control parameters did not impact the SNR significantly as shown in Fig. S5. The target concentrations did not affect the dwell times and peak amplitudes much, which can also be inferred from distributions of interval time. However, the normalized event frequency increased with the increasing target concentration as anticipated. The test conditions studied here limit the number of tested hydrogel samples to three for establishing no significant impact on the translocation characteristics of a 200 bp dsDNA target. These experiments were not conducted on short DNA fragments with target lengths other than 200 bp, as they will only contribute to the target length dependent increase or decrease in blockade amplitude and dwell times. Having analyzed the effect of these control parameters, we next performed sizing of dsDNA fragments with different lengths.

3.4. dsDNA size resolution of HIGN

To determine the size resolution of our hydrogel-assisted nanopore, we tested dsDNA target molecules of 50, 100, 150, 200, 250, 300, and 400 bp length. All the dsDNA targets were prepared separately in a 4 M LiCl measurement buffer at 0.1 fM concentration, and each target solution in the separate nanopore was individually analyzed with HIGN at an applied bias of -0.2 V . Each nanopore with respective target DNA solution was inserted in the hydrogel at location L1 and depth D2 previously described in “Section 3.3”. The current-time (I - t) data was logged in a custom LabVIEW program. The representative I - t traces and scatter populations for the different length DNA molecules have been shown in Fig. 4a. To obtain event scatter populations, the blockade amplitudes and dwell times were recorded above six times the root mean square (rms) noise from the baseline current for each target. The current blockade amplitude is expected to increase with the bp target length as the DNA molecules thread through the nanopore into the hydrogel. This phenomena has been discussed by (Al Sulaiman et al., 2018) using a hydrogel model comprised of a matrix of interconnected pores in layered architecture forcing linear thread-like translocations of nanopores. So, when the DNA molecules of increasing bp (50–400) sizes translocate from the nanopore into the hydrogel, they cause blockage of these interconnected pores of the hydrogel in a size dependent manner. To ensure negligible pore size variations, each nanopore with the target solution was first analyzed in bare 4 M LiCl solution and the baseline current was confirmed to be $\sim -1.7 \pm 0.2\text{ nm}$ before inserting in the hydrogel. However, still due to the heterogeneity of the hydrogel and nanopores, which may cause slight shifts in baseline current and the nanopore noise, we evaluated the normalized peak amplitudes ($\Delta I/I_0$) instead of the blockade amplitudes. An increase in $\Delta I/I_0$ was observed as the target DNA length increased which is evident from the shift in scatter populations on $\Delta I/I_0$ axis. The I - t traces show might not show a direct significant increase in the blockade amplitudes because all the different length molecules have been tested with separate nanopores thereby having slightly different baseline currents. There were no significant shifts of the populations on the dwell time scale, so only the counts’ distributions for $\Delta I/I_0$ were fitted by the gaussian functions as shown in Fig. 4b. A shift in mean $\Delta I/I_0$ can also be observed on the gaussian overlays of the counts histograms as the DNA size increases. A linear fit ($r^2 \approx 0.99$) to the mean $\Delta I/I_0$ as a function of DNA bp size shown in Fig. 4c suggests a sensitivity of ~ 0.0001 of $\Delta I/I_0$ change per bp length (data presented as $\mu \pm \sigma$, $n = 3$). This implied that our HIGN could resolve 50 bp with $\Delta I/I_0$ of ~ 0.005 . The high resolution of our HIGN led us to explore its applicability in the label-free multiplexed detection of infectious agents from multiplexed RT-PCR.

3.5. HIGN for multiplexed detection of IAV and SARS-CoV-2

As our HIGN is capable of sizing short DNA fragments with high resolution, we were able to perform HIGN based single plex and multiplexed detection of RT-PCR assay products of respiratory infectious agents: Influenza A Virus (IAV) and severe acute respiratory syndrome coronavirus 2 (SARS-CoV-2) instead of previously adapted RT-LAMP (Tang et al., 2022) for producing longer amplicons. For this purpose, the single plex and multiplexed RT-PCR assays were performed with their respective no template controls (NTC): NTC1 for IAV, NTC2 for SARS-CoV-2, and NTC3 for IAV + SARS-CoV-2. The RT-PCR assay details have been described in “Materials and Methods” section 2.5. The primers for IAV and SARS-CoV-2 were designed to produce RT-PCR amplicons of sizes 146 bp and 72 bp respectively with a size difference of 74 bp which was above 50 bp sizing resolution of our HIGN. For reliable sizing of more than two targets, amplicon sizes should maintain size differences of more than the sizing resolution of HIGN.

The endpoint RT-PCR assay was performed according to the established protocol followed by gel-electrophoresis using 5% agarose gel and gel-imaging. The result of the gel image in Fig. 5a shows the gel bands

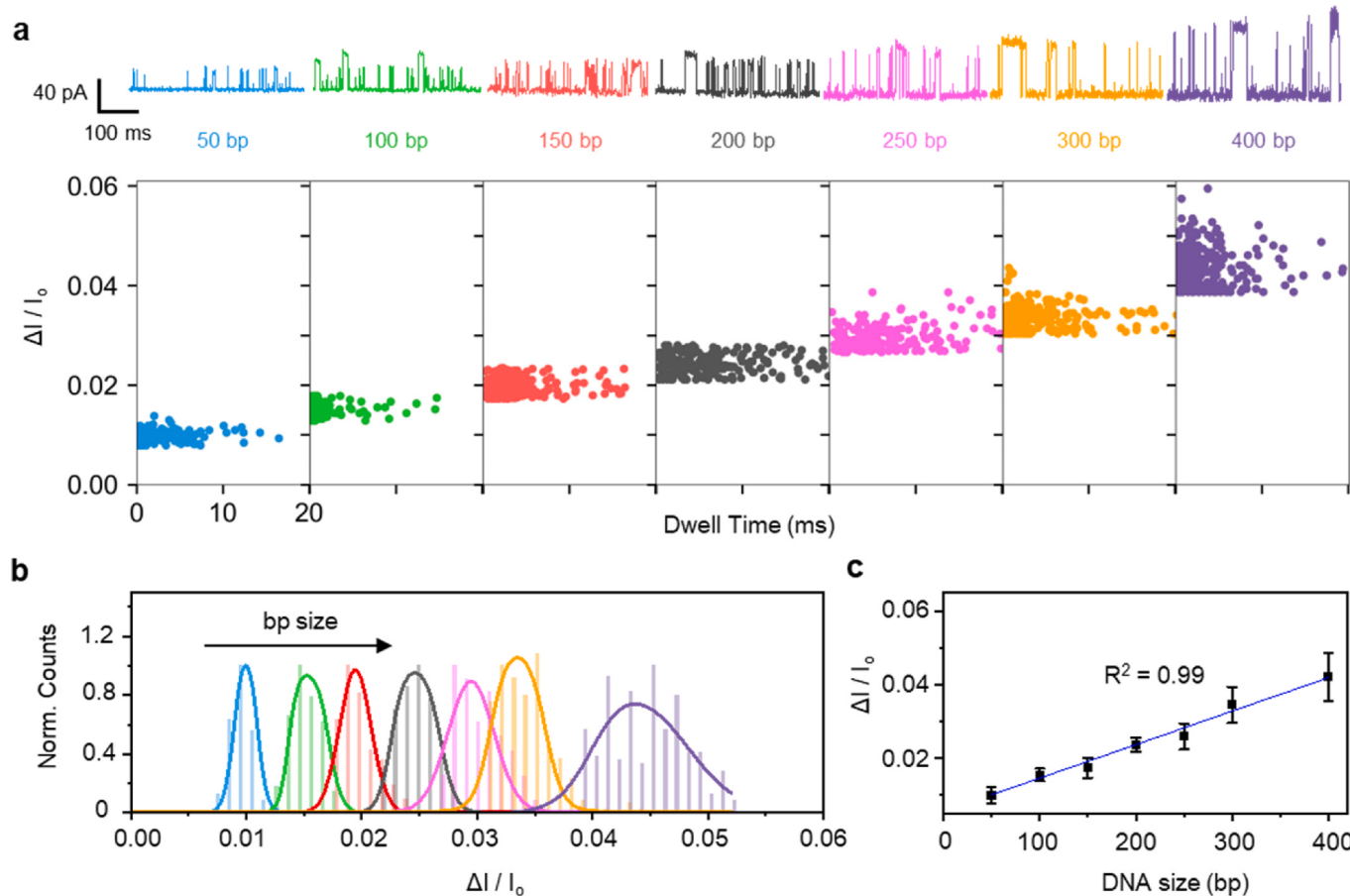


Fig. 4. Size resolution of HIGN: Size counting analysis of NA fragments with different bp lengths (50 – 400 bp); (a) Representative I-t traces with event scatter populations for different length targets. (b) A combined histogram with respective gaussian fittings shows the right shift of mean normalized peak amplitudes for increasing dsDNA bp size. (c) A linear fit to the normalized blockage amplitudes versus bp size of dsDNA, data has been presented as $\mu \pm \sigma$ for $n = 3$.

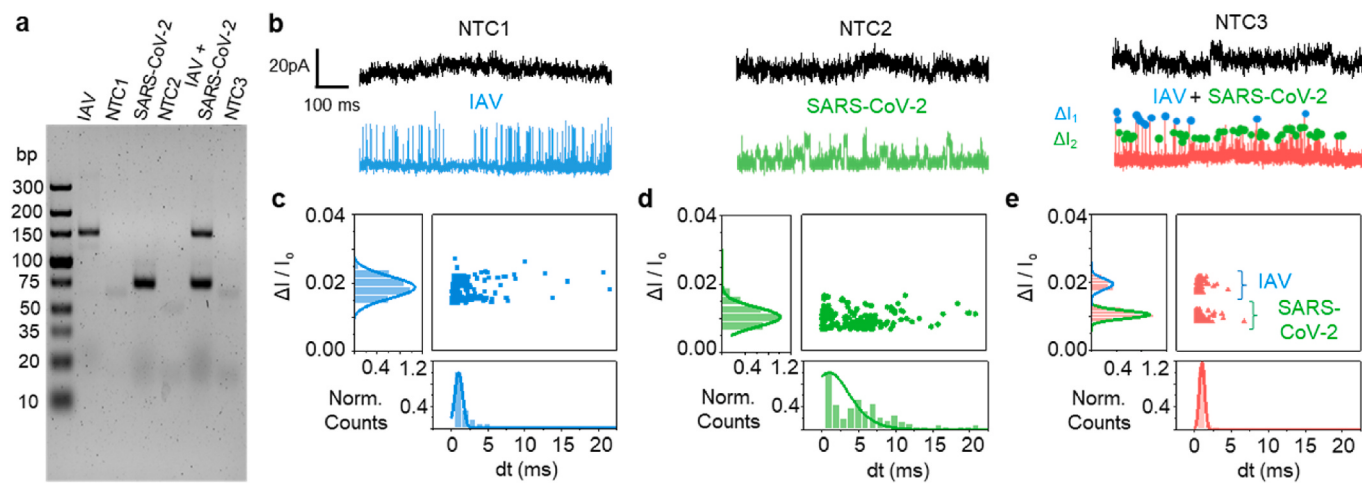


Fig. 5. Multiplexed detection of IAV and SARS-CoV-2: (a) Gel-electrophoresis image of single plex (IAV and SARS-CoV-2) and multiplexed (IAV + SARS-CoV-2) RT-PCR assays, (b) I-t traces for HIGN analysis of single plex and multiplexed IAV and SARS-CoV-2 RT-PCR products, scatter data and counts distributions for (c) IAV single plex RT-PCR assay, $N_1 = 271$, $\mu_1 \approx 0.019$, $\sigma_1 \approx 0.026$, (d) SARS-CoV-2 single plex RT-PCR assay, $N_2 = 156$, $\mu_2 \approx 0.01$, $\sigma_2 \approx 0.0026$, (e) Multiplexed (IAV + SARS-CoV-2) RT-PCR assay using HIGN, $N_1 = 164$, $N_2 = 333$ $N_{\text{total}} = 497$.

for amplicons located at ~146 bp and ~72 bp for single plex IAV and single plex SARS-CoV-2 assays, respectively. Similarly, both the bands were present for multiplexed assay with no bands for all NTCs. Post RT-PCR, the reaction concentrations were estimated to be ~30.51 μM and ~61.08 μM , which were diluted to bring down to ~0.1 fM in 4 M LiCl for

detection with our HIGN. The HIGN experiments for RT-PCR products were conducted at a fixed insertion location, depth (~60 μm), and applied bias -0.2 V. All the I-t traces for positive and negative controls have been given in Fig. 5b. The HIGN scatter population ($N_1 = 271$) data for single plex IAV RT-PCR assay has been shown in Fig. 5c with

corresponding counts distributions of $\Delta I/I_0$ and dwell times. The scatter population is well positioned on $\Delta I/I_0$ scale for 146 bp amplicons reciprocating its expected position from Fig. 4b. No target translocations were detected in NTC1 as expected as can be seen from Fig. 5b with uniform amplitudes for 146 bp IAV amplicons and high event frequency. Similarly, the HIGN data for SARS-CoV-2 in Fig. 5d shows scatter population ($N_2 = 156$) for translocations of 72 bp amplicons positioned accordingly on a $\Delta I/I_0$ scale with respective counts distributions of $\Delta I/I_0$ and dwell times with respective $I-t$ traces for SARS-CoV-2 positive control and NTC2 in Fig. 5b. NTC2 also did not show any translocations as expected. The normalized peak amplitude ($\Delta I/I_0$) counts distribution suggested a mean of 0.01 for 72 bp amplicons (as compared to 0.019 for 146 bp IAV amplicons) making them clearly distinguishable. Our HIGN reliably performed size counting on single plex IAV and SARS-CoV-2 RT-PCR products.

For the multiplexed assay, both the amplicons of IAV and SARS-CoV-2 were present in the multiplexed RT-PCR product. To analyze the nanopore data of multiplexed RT-PCR product, two separate blockage current amplitudes ($\Delta I_1, \Delta I_2$) were defined using $\mu \pm \sigma$ from previously obtained means and standard deviations of the single plex IAV (μ_1, σ_1) and SARS-CoV-2 (μ_2, σ_2) HIGN scatter data. The scatter data for multiplexed RT-PCR has also been shown in Fig. 5e with associated counts distributions of $\Delta I/I_0$ and dwell times. Two scatter populations are clearly distinguishable on $\Delta I/I_0$ scale corresponding to 146 bp (IAV) amplicons and 72 bp (SARS-CoV-2) amplicons with corresponding event markings in $I-t$ trace shown in Fig. 5b. Interestingly, $\Delta I/I_0$ the counts' distributions also suggest higher relative abundance for 72 bp SARS-CoV-2 target amplicons ($N_2 = 333$) as compared to 146 bp IAV target amplicons ($N_1 = 164$), which agrees with their initial stock concentrations of 2×10^4 cp/ μL and 10^4 cp/ μL , respectively. The dwell times were quite shorter as compared to individual single plex assays, which can be associated with the slightly bigger nanopore diameter or hydrogel mesh size at the interface. Nonetheless, our HIGN effectively distinguished the IAV and SARS-CoV-2 from multiplexed RT-PCR assay, suggesting its high potential for future label-free multiplexed detection applications.

4. Conclusion

In this work, we have examined a facile PEG-DMA hydrogel interfaced glass nanopore (HIGN) platform for high resolution sizing of short DNA fragments in 50–400 bp range. A $\sim 11 \times$ increase in mean dwell times was observed as compared to a bare solution nanopore when 200 bp dsDNA molecules encountered entropic barriers offered by the PEG-DMA hydrogel mesh fibers at the hydrogel nanopore interface. A glass nanopore with ~ 10 nm diameter when inserted in 5, 7.5 and 10% w/v hydrogels, suggested higher mean dwell times, peak amplitudes, and frequency as the % w/v increased from 5 to 7.5% w/v (with estimated mesh sizes ξ from 15 to 7 nm respectively). Whereas 10% hydrogel caused frequent clogging due to poor degree of swelling. The detailed investigation on the spatial placements of 10 nm glass nanopore into the 7.5% w/v hydrogel suggested a negligible effect on the translocation characteristics of 200 bp dsDNA. Different insertion locations and depths resulted in CV of 7.16% and 5.28% respectively for mean normalized event frequencies. Whereas increasing applied bias voltage and DNA concentrations at fixed insertion locations and depths linearly increased the event frequencies as expected. Examining dsDNA fragments of 50–400 bp lengths showed increasing mean normalized peak amplitudes ($\Delta I/I_0$) in length dependent manner, with an achieved 50 bp resolution producing $\Delta I/I_0$ of ~ 0.005 . This led us to explore the applicability of our HIGN for the successful label-free multiplexed detection of globally prevalent IAV and SARS-CoV-2 respiratory infections from multiplexed RT-PCR. Our high-resolution HIGN resulted in $\Delta I/I_0$ of 0.019 and 0.01 for IAV (amplicon length: ~ 146 bp) and SARS-CoV-2 (amplicon length: ~ 72 bp) respectively, clearly distinguishing them in a multiplexed reaction. With its propitious capabilities, we anticipate that the HIGN system has a high potential for label-free multiplexed

molecular diagnostic applications.

CRediT authorship contribution statement

Muhammad Asad Ullah Khalid: Writing – review & editing, Writing – original draft, Methodology, Investigation, Formal analysis, Conceptualization. **Md. Ahsan Ahamed:** Writing – original draft, Visualization, Investigation, Formal analysis. **Ming Dong:** Software, Methodology, Formal analysis. **Aneesh Kshirsagar:** Methodology, Investigation, Formal analysis. **Weihua Guan:** Writing – review & editing, Supervision, Resources, Funding acquisition, Conceptualization.

Declaration of competing interest

The authors declare that they have no known competing financial interests or personal relationships that could have appeared to influence the work reported in this paper.

Acknowledgments

This work was partially supported by the National Science Foundation (2045169, 2319913), and the American Rescue Plan Act through USDA APHIS (APHIS/NIFA Collaborative award# 2023-70432-41395). Any opinions, findings, conclusions, or recommendations expressed in this work are those of the authors and do not necessarily reflect the views of the National Science Foundation and USDA.

Appendix A. Supplementary data

Supplementary data to this article can be found online at <https://doi.org/10.1016/j.bios.2024.116895>.

Data availability

Data will be made available on request.

References

- Acharya, S., Jiang, A., Kuo, C., Nazarian, R., Li, K., Ma, A., Siegal, B., Toh, C., Schmidt, J. J., 2020. ACS Sens. 5, 370–376. <https://doi.org/10.1021/acssensors.9b01928>.
- Ahamed, M.A., Khalid, M.A.U., Dong, M., Politza, A.J., Zhang, Z., Kshirsagar, A., Liu, T., Guan, W., 2023. Biosens. Bioelectron. 115866. <https://doi.org/10.1016/j.bios.2023.115866>.
- Al Sulaiman, D., Cadinu, P., Ivanov, A.P., Edel, J.B., Ladame, S., 2018. Nano Lett. 18, 6084–6093. <https://doi.org/10.1021/acs.nanolett.8b03111>.
- Al Sulaiman, D., Gatehouse, A., Ivanov, A.P., Edel, J.B., Ladame, S., 2021. ACS Appl. Mater. Interfaces 13, 26673–26681. <https://doi.org/10.1021/acsami.1c01145>.
- Barrio, P.A., Fernández-Rodríguez, A., Martín, P., Fernández, C., Fernández, L., Alonso, A., 2021. Forensic Sci. Int. 323, 110775. <https://doi.org/10.1016/j.forsciint.2021.110775>.
- Boutonnet, A., Pradines, A., Mano, M., Kreczman-Brun, M., Mazières, J., Favre, G., Ginot, F., 2023. Anal. Chem. 95, 9263–9270. <https://doi.org/10.1021/acs.analchem.3c00998>.
- Burke, G., Barron, V., Geever, T., Geever, L., Devine, D.M., Higginbotham, C.L., 2019. J. Mech. Behav. Biomed. Mater. 99, 1–10. <https://doi.org/10.1016/j.jmbbm.2019.07.003>.
- Carr, D.A., Peppas, N.A., 2009. Macromol. Biosci. 9, 497–505. <https://doi.org/10.1002/mabi.200800235>.
- Chau, C., Marcuccio, F., Soulias, D., Edwards, M.A., Tuplin, A., Radford, S.E., Hewitt, E., Actis, P., 2022. ACS Nano 16, 20075–20085. <https://doi.org/10.1021/acsnano.2c08312>.
- Chau, C.C., Radford, S.E., Hewitt, E.W., Actis, P., 2020. Nano Lett. 20, 5553–5561. <https://doi.org/10.1021/acs.nanolett.0c02246>.
- Chung, M., Kim, D., Herr, A.E., 2014. The Analyst 139, 5635–5654. <https://doi.org/10.1039/C4AN01179A>.
- Di Lorenzo, F., Seiffert, S., 2015. Polym. Chem. 6, 5515–5528. <https://doi.org/10.1039/C4PY01677G>.
- Dong, M., Tang, Z.F., Hicks, S., Guan, W.H., 2022. Anal. Chem. 94, 3865–3871. <https://doi.org/10.1021/acs.analchem.1c04781>.
- Folgea, D., Uplinger, J., Thomas, B., McNabb, D.S., Li, J., 2005. Nano Lett. 5, 1734–1737.
- Fonfara, I., Richter, H., Bratovic, M., Le Rhun, A., Charpentier, E., 2016. Nature 532, 517. <https://doi.org/10.1038/nature17945>.

- Fragasso, A., Schmid, S., Dekker, C., 2020. *ACS Nano* 14, 1338–1349.
- Fu, J.P., Mao, P., Han, J., 2008. Trends Biotechnol. 26, 311–320. <https://doi.org/10.1016/j.tibtech.2008.02.009>.
- Green, M.R., Sambrook, J., 2019. Cold Spring Harb. Protoc. 2019. <https://doi.org/10.1101/pdb.top100388> pdb.top.100388.
- Harstad, R.K., Johnson, A.C., Weisenberger, M.M., Bowser, M.T., 2016. *Anal. Chem.* 88, 299–319. <https://doi.org/10.1021/acs.analchem.5b04125>.
- Hashem, V., Tiwari, A., Bewick, B., Teive, H.A.G., Moscovitch, M., Schuele, B., Bushara, K., Bower, M., Rasmussen, A., Tsai, Y.C., Clark, T., McFarland, K., Ashizawa, T., 2020. *PLoS One* 15. <https://doi.org/10.1371/journal.pone.0228789>. ARTNe0228789.
- Head, S.R., Komori, H.K., LaMere, S.A., Whisenant, T., Van Nieuwerburgh, F., Salomon, D.R., Ordoukhianian, P., 2014. *Biotechniques*. <https://doi.org/10.2144/000114133>, 56, 61–+.
- Herschleb, J., Ananiev, G., Schwartz, D.C., 2007. *Nat. Protoc.* 2, 677–684. <https://doi.org/10.1038/nprot.2007.94>.
- Khatri, S., Pandey, P., Mejia, G., Ghimire, G., Leng, F., He, J., 2023. *J. Am. Chem. Soc.* 145, 28075–28084. <https://doi.org/10.1021/jacs.3c09311>.
- Kowalczyk, S.W., Wells, D.B., Aksimentiev, A., Dekker, C., 2012. *Nano Lett.* 12, 1038–1044. <https://doi.org/10.1021/nl204273h>.
- Kubo, T., Arimura, S., Tominaga, Y., Naito, T., Hosoya, K., Otsuka, K., 2015. *Macromolecules* 48, 4081–4087. <https://doi.org/10.1021/acs.macromol.5b00834>.
- Lalitha Sridhar, S., Schneider, M.C., Chu, S., De Roucy, G., Bryant, S.J., Vernerey, F.J., 2017. *Soft Matter* 13, 4841–4855. <https://doi.org/10.1039/C7SM00423K>.
- Larkin, J., Henley, R.Y., Muthukumar, M., Rosenstein, J.K., Wanunu, M., 2014. *Biophys. J.* 106, 696–704. <https://doi.org/10.1016/j.bpj.2013.12.025>.
- Lastra, L.S., Bandara, Y.M.N.D.Y., Nguyen, M., Farajpour, N., Freedman, K.J., 2022. *Nat. Commun.* 13, 2186. <https://doi.org/10.1038/s41467-022-29758-8>.
- Lee, J.-S., Kim, M., Seong, M.-W., Kim, H.-S., Lee, Y.K., Kang, H.J., 2020. *Clin. Chem. Lab. Med.* CCLM 58, 527–532. <https://doi.org/10.1515/cclm-2019-0896>.
- Li, H., Li, Y., Gui, C., Chen, D., Chen, L., Luo, L., Huang, G., Yuan, Y., He, R., Xia, F., Wang, J., 2023. *Talanta* 256, 124275. <https://doi.org/10.1016/j.talanta.2023.124275>.
- Li, M., Yin, F., Song, L., Mao, X., Li, F., Fan, C., Zuo, X., Xia, Q., 2021. *Chem. Rev.* 121, 10469–10558. <https://doi.org/10.1021/acs.chemrev.1c00241>.
- Malo De Molina, P., Lad, S., Helgeson, M.E., 2015. *Macromolecules* 48, 5402–5411. <https://doi.org/10.1021/acs.macromol.5b01115>.
- McCord, B.R., Gauthier, Q., Cho, S., Roig, M.N., Gibson-Daw, G.C., Young, B., Taglia, F., Zapico, S.C., Mariot, R.F., Lee, S.B., Duncan, G., 2019. *Anal. Chem.* 91, 673–688. <https://doi.org/10.1021/acs.analchem.8b05318>.
- Mouliere, F., Rosenfeld, N., 2015. *Proc. Natl. Acad. Sci.* 112, 3178–3179. <https://doi.org/10.1073/pnas.1501321112>.
- Nouri, R., Tang, Z., Guan, W., 2019. *Anal. Chem.* 91, 11178–11184. <https://doi.org/10.1021/acs.analchem.9b01924>.
- Rabinowitz, J., Edwards, M.A., Whittier, E., Jayant, K., Shepard, K.L., 2019. *J. Phys. Chem. A* 123, 8285–8293. <https://doi.org/10.1021/acs.jpca.9b04075>.
- Sanchez, C., Roch, B., Mazard, T., Blache, P., Dache, Z.A., Pastor, B., Pisareva, E., Tanos, R., Thierry, A.R., 2021. *Jci Insight* 6. <https://doi.org/10.1172/jci.insight.144561>. ARTNe144561.
- Tang, Z.F., Nouri, R., Dong, M., Yang, J.B., Greene, W., Zhu, Y.S., Yon, M., Nair, M.S., Kuchipudi, S.V., Guan, W.H., 2022. *Biosens. Bioelectron.* 197. <https://doi.org/10.1016/j.bios.2021.113759>. ARTn113759.
- Ungerer, V., Bronkhorst, A.J., Uhlig, C., Holdenrieder, S., 2022. *Diagnostics* 12, 1896. <https://doi.org/10.3390/diagnostics12081896>.
- Venkatesan, B.M., Bashir, R., 2011. Springer US, Boston, MA. https://doi.org/10.1007/978-1-4419-8252-0_1.
- Yusko, E.C., An, R., Mayer, M., 2010. *ACS Nano* 4, 477–487. <https://doi.org/10.1021/nm9013438>.